RSC Advances

ROYAL SOCIETY OF CHEMISTRY

www.rsc.org/advances

Large-scale fabrication of porous bulk silver thin sheets with tunable porosity for high-performance binder-free supercapacitor electrodes†

Xiangyu Wang, Pinghui Zhang, Sascha Vongehr, Shaochun Tang,* Yongguang Wang, Xiangkang Meng*

Institute of Materials Engineering, National Laboratory of Solid State Microstructures, and College of Engineering Applied Sciences, Nanjing University, Jiangsu, P. R. China

* Correspondence and requests for materials should be addressed to S.C. Tang (tangsc@nju.edu.cn) or X.K. Meng (mengxk@nju.edu.cn).

Abstract

We report a novel method for the large-scale fabrication of porous bulk silver thin sheets (PSTS) built from three-dimensionally interconnected nanoparticles (NPs). The synthesis starts with synthesizing silver sponges via an *in situ* growth of NPs which assemble into networks. The sponges are pressed into thin sheets before etching in acid. The resulting porosity is nearly homogeneous throughout the whole volume. The dependence on acid concentration was investigated and the average pore diameter can be controlled in a range of 83~145 nm by etching time. Growing metal oxides results in PSTS/Co_3O_4 composites which can be used directly as binder-free supercapacitor electrodes. The Co_3O_4 growth is optimized and the optimized composite electrode provides a much higher specific capacitance (1276 F g^{-1} at 1 A g^{-1}) than previously reported for pure Co_3O_4 nanostructures with different shapes or those for Ag-Co_3O_4 composite nanowire array electrodes. The optimal electrode has a superior rate capability (still 986 F g^{-1} at 10 A g^{-1}). The improvements are attributed to the continuous open porosity of PSTS and a direct contact between Co_3O_4 and Ag ligaments. The method can be extended to many other metals or alloys, promising wide application.

Keywords: Porous metals; silver; size control; chemical etching; supercapacitors

1. Introduction

Nanoporous metals combine prominent thermal and electrical conductivity, ductility and high catalytic activity with porous architectures' high surface area and low density.[1-3] They thus have a wide range of applications in catalysis,[4] sensing,[5] photonics,[6] and so on. Especially, they have unique advantages as substrates of many high capacitive but nonconductive metal oxides for energy storage,[7] namely providing high conductivity for electron transfer,[8] a three-dimensionally interconnected porous nanostructure for rapid ion diffusion,[9] and a large surface area for charge storage.[10]

Reported strategies to prepare nanoporous metals mainly include templating,[11] dealloying,[12] combustion,[13] sol-gel assembly,[14] electrochemical etching,[15] and laser ablation.[16] Templating based on the replication of inorganic and polymeric templates can precisely control the pores and ligaments' sizes as well as surface morphology at the nanoscale,[17] but is generally too demanding, time consuming, and expensive. For example, the infiltration of metal precursors into the templates is difficult.[18] Dealloying by chemical or electrochemical etching to selectively dissolve one or more of the elemental components has become one of the most efficient methods.[12,19] However, the porous structure generally has a large variation in pore size and porosity due to the presence of multiple intermetallic phases.[20] To obtain a uniform porosity, the alloy must have constant metal ratios throughout. In addition, there are still some difficulties in controlling nanostructure and tuning properties due to narrow composition ranges of the alloy precursors.[21]

Silver has the highest conductivity among the noble metals. Porous silver is one of the most important materials, especially for such applications as energy storage, surface-enhanced Raman scattering, and catalysis.[22-26] Recent reports on porous silver nanostructures mainly focus on powders.[27] Due to the low stability of Ag and Ag-based materials,[28] few reports have focused on a large-scale fabrication of bulk nanoporous silver, especially to achieve such material with uniform, continuous open porosity and controlled sizes for electrode applications is still a challenge. Here, we report a novel method for large-scale fabrication of porous silver thin sheets (PSTS) composed of 3D interconnected nanoparticles (NPs) by a three-step procedure (scheme 1): synthesis of silver nanosponges, pressing the sponges into bulk thin sheets, and etching in HNO_3. It is demonstrated that uniform PSTS cannot be achieved if instead using commercial silver sheets or even ones obtained from pressing NPs into sheets. Our approach is capable of obtaining PSTS with tunable NPs' diameters and pore sizes. The time and concentration dependent etching is systematically investigated. To demonstrate the potential for applications, we synthesized composites by hydrothermal growth of Co_3O_4 on the ligaments of the PSTS. The PSTS/Co_3O_4 composites can be directly used as binder-free supercapacitor electrodes. An optimization of Co_3O_4 content results in a high specific capacitance of 1276 F g^{-1} at 1 A g^{-1} and a superior rate capability (still 986 F g^{-1} at 10 A g^{-1}). The specific capacitance of Co_3O_4 is demonstrated to be much improved comparing with the reported values for pure Co_3O_4 nanostructures and Ag-Co_3O_4 composites. The reasons for the property improvement are also discussed.

2. Experimental section

2.1. Synthesis of PSTS

The preparation of PSTS is illustrated in scheme 1. Silver sponges were prepared first. Typically, 5 mL $AgNO_3$ aqueous solution with a concentration of 0.1 M was rapidly injected into 25 mL water-glycerol (volume ratio was 4:1) mixed $NaBH_4$ solution (0.1 M) during a fast stir. The high viscosity glycerol reduces the mobility of the later suspended NPs in order to prevent their excessive aggregation. Also H_2 nanobubbles from the $NaBH_4$ prevents NPs' aggregating and is crucial for the network-like structures later obtained. Stirring was continued until the solution became colorless (~ 5 min). The product was obtained by filtering, washed, and freeze dried. Then, 80 mg dried silver sponge powder was pressed into a round thin silver sheet with a diameter of 10 mm on a manual powder compressor (769YP-100G) under 10 kN for 30 seconds. For comparison, isolated silver NPs were prepared by a previously reported microwave assisted method[29] and also pressed into bulk thin sheets. Commercial silver sheets (purity⩾99.8%) were obtained from Chemical Reagent Co., Ltd., National Pharmaceutical Group, China. All the sheets were put into diluted HNO_3 aqueous solutions at room temperature. The etched sheets were washed and dried in air.

2.2. Synthesis of PSTS/Co_3O_4 composites

$Co(NO_3)_2$ solutions with the concentrations of 5.0, 8.0, 10, and 20 mM were prepared in water-ethanol mixture (volume ratio was 6:1). Cetyltrimethylammonium bromide was added, resulting in a 2 mM concentration. Then, 35 ml of this solution was transferred to a Teflon-lined stainless steel autoclave with a total volume of 50 ml. After rinsing the PSTS with acetone, ethanol and deionized water (18.2 MΩ cm) sequentially, they were fixed with a plastic clamp inside the autoclave. The sealed autoclave was held for 90 min at 120 °C. After cooling to room temperature, the PSTS/Co_3O_4 composites were washed with deionized water and dried in air.

2.3. Characterizations

Morphology and microstructure were analyzed by scanning electron microscopy (SEM) with a Sirion XL, FEI, Hillsboro, OR, USA at 10 kV accelerating voltage. Average pore and nanoparticle diameters were determined from 50 samples randomly chosen in SEM images. Composition and crystallographic properties of the products were investigated by X-ray diffraction (XRD) on a Rigaku Ultima III diffractometer using Cu $K\alpha$ = 1.5418 Å radiation. Specific surface area (SSA) of the PSTS was measured by a Brunauer-Emmett-Teller (BET) method, which was conducted on an automatic volumetric adsorption analyzer (Quantachrome Instruments, USA).

2.4. Electrochemical measurements

Electrochemical measurements were carried out using a computer controlled CH1660D electrochemical workstation. All substrate areas are 0.79 cm^2, but the area immersed into the electrolyte was 0.4 cm^2, leaving the area above for connection clamps. Cyclic voltammetry (CV) and galvanostatic charge-discharge (CD) measurements were conducted in a three-electrode cell where a Pt electrode serves as the counter electrode and a standard Ag/AgCl electrode as reference, all in 2.0 M KOH aqueous solution as electrolyte. Gravimetric specific capacitances were calculated from the discharging curves according to $C_s = (I\Delta t)/(m\Delta V)$, where I is current, Δt is the discharge time, m the mass of active material, and ΔV the voltage drop at discharge.

3. Results and discussion

Fig. 1a shows a photograph of a PSTS from a typical synthesis, defined as etching of pressed thin sheet with 16% concentrated HNO_3 for 5 minutes. From a high magnification top-view SEM image (Fig. 1b), one can see that the sheet has a uniform porosity over the whole surface. Also, the pores are clearly larger than before etching (comparing with Fig. S1 in supporting information). A magnified SEM image (Fig. 1c) reveals a continuously interconnected network having also all pores inter-connected. The ligaments of the network consist of NPs with an average diameter of ~ 72 nm. Fig. 1d-f shows the cross section of broken PSTS. The thickness of the sheet is about 123 μm (Fig. 1d). Magnified SEM (Fig. 1e) shows similar porosity, indicating that the etching occurred throughout the interior of the sheet. Further magnification (Fig. 1f) shows that the NPs are no longer clearly visible in the inside of the sheet. The inset shows the size distribution of pore diameters; the average diameter is 90.5 nm. Using instead a silver sheet obtained by pressing silver NPs, the resulting product is composed of NPs aggregations without continuous ligaments (see Fig. S2a). The structure is also much more brittle. When commercial silver sheets were used instead, a far less uniform, rough surface consisting of irregularly shaped sheets is obtained (see Fig. S2b).

When the HNO_3 concentration is doubled to 32% (Fig. 2a), the surface pores diameters are much more broadly distributed with some pores being very large. At 20%, a few large pores are still present, as shown in Fig. 2b, but it more closely resembles the typical result at 16%. At 10% HNO_3 concentration (Fig. 2c), the surface is flatter, and local magnification (see inset) shows that the pore network is much less accessible. At 5%, the originally smooth surface is hardly transformed at all (Fig. 2d), and the etching does not proceed any further even after 1 h, as shown in a magnified image (inset of Fig. 2d). The etching rate is faster at higher temperature (60 ^{o}C), but this leads to very inhomogeneous etching with very large pores (not shown). At room temperature and moderate (typical) concentration, the reaction can be controlled via the etching time. Fig. 3 shows the surface morphology of PSTS after etching with 16% HNO_3 for 1 to 4 minutes. The most obvious is the gradual thinning of the ligaments. After 6 min etching, the porous structure starts to collapse. Fig. 4 shows the particle and pore diameters versus etching time ranging from 1 to 5 min. The average pore size increases from 83 to 145 nm. Note that particle diameter and pore sizes are not independent. The pores grow directly as a consequence of that the NPs shrink. Therefore, the two data points at 3 minutes in Fig. 4, which create the appearance of plateaus between 2 to 3 minutes, come both from the single fact of that the 3 min etching alone is somewhat of an outlier.

The formation of PSTS via chemical etching is illustrated in scheme 2. At the initial stage, metal bonds between silver atoms are destroyed by a reaction $3Ag + 4HNO_3$ (diluted) $= 3AgNO_3 + 2H_2O + NO\uparrow$, and corrosion reactions at the solid/liquid interface occur, which results in that PSTS surface close to liquid starts to be dissolved at first (surface etching) and surface pores form immediately (Fig. 3a). As the corrosion process continues, more diluted HNO_3 enters the interior of the porous thin sheet through gaps between adjacent silver chains whose morphology was remained during the physical compression of sponges (silver sponges consist of interconnected nanochains), and inner etching happens. At the same time, the surface pores are getting larger and larger, leading to the formation of islands-like ligaments (Fig. 3b). With continuous metal bond interrupting and atoms diffusion, the surface NPs and chains inside both become smaller and smaller, which results in thinning and surface smoothing of the ligaments and a PSTS with 3D network nanostructure is formed (Fig. 3d).

We fabricated PSTS/Co_3O_4 composites by growing Co_3O_4 onto the ligaments of the PSTS. Fig. S3 in supporting information shows XRD pattern of the PSTS/Co_3O_4 composite obtained with a Co^{2+} concentration of 20 mM. Diffraction peaks can be assigned to the (220), (311), (222), (400), (422), (440), and (533) planes of spinel-type Co_3O_4 (JCPDS No. 42-1467),[30] apart from two significant diffraction peaks attributed to the (200) and (311) reflections of face-centered cubic silver (JCPDS No. 04-783), demonstrating the formation of Ag/Co_3O_4 composites. The amount of Co_3O_4 increases with the concentration of $Co(NO_3)_2$. The Co_3O_4 loadings are 1.4, 2.9, 3.8 and 6.6 mg/cm^2 at $Co(NO_3)_2$ concentrations of 5, 8, 10, and 20 mM, respectively. At a low concentration of 1 mM Co^{2+}, only a few Co_3O_4 particles cover a small part of the Ag ligaments' surfaces (Fig. 5a). When Co^{2+} concentration increases to 8 mM, Co_3O_4 grows along the silver ligaments (Fig. 5b). The coverage is composed of nanocrystals with diameters of 5~20 nm. This indicates that the Co_3O_4 has end-bonded contacts with the ligaments,[7] offering excellent electrical conductivity between Ag and Co_3O_4. When the Co^{2+} concentration doubles to 16 mM, Co_3O_4 grows into larger NPs, but most of the newly added particles have not grown on the Ag ligaments (Fig. 5c). Further increasing Co^{2+} concentration to 20 mM results in more Co_3O_4 NPs, but the additional particles add on top of the already grown active material instead of contacting the ligaments. Also, large Co_3O_4 aggregates start to seal the porous structure (Fig. 5d).

We explored potential application of the PSTS/Co_3O_4 composites via a direct use as electrodes for supercapacitors. The direct coating of 3D continuous porous Ag facilitates integration of porous metal/oxide composites with current collectors without any additional contact resistance.[31] Fig. 6a shows CV curves measured at 5 mV s^{-1} of the PSTS/Co_3O_4 electrodes with different Co_3O_4 loadings. They imply pseudocapacitance and maximum specific capacitance is obtained at a loading of 2.9 mg/cm^2. The corresponding galvanostatic discharging curves measured at 1.0 A g^{-1} are shown in Fig. 6b. Maximum performance should be expected when any further addition of active material will add on top of already present Co_3O_4, because (1) it then has no direct conductive contact to the metal and (2) it decreases electrolyte access to the Co_3O_4 below. The discharge time of the composite with a loading of 2.9 mg/cm^2 is the longest (180 seconds), indicating maximum capacitance, which is consistent with the CV results. Fig. 6c shows the corresponding C_s values. The performance increases steeply as Co_3O_4 is added, because the bare Ag structure is not capacitive. As seen in SEM images, a continuous coating around all ligaments is never achieved; a critical coating thickness[32,33] is therefore not found. The electrochemical properties of pure Co_3O_4 nanomaterials depend crucially on morphology and sizes, so one cannot meaningfully compare to any standard pure Co_3O_4 material. Therefore, we compare with published reports. C_s at 8 mM reaches 1276 F g^{-1}, which is usually more than double the previously reported 90 to 680 F g^{-1} (all at 1 A g^{-1}) for pure Co_3O_4 with various morphologies including NPs,[34] nanosheets,[35] hollow spheres,[36] nanotubes,[37] porous hexagons,[38] and 3D hierarchical nanostructures.[39,40] It is also superior to Co_3O_4 nanowire arrays on Ni foam (444 F g^{-1}),[41] and Ag doped Co_3O_4 nanowire arrays.[42] The capacitance of 1139 F g^{-1} at 2 A g^{-1} is still higher than that for Co_3O_4-Ag nanowire array electrodes (1006 F g^{-1} also at 2 A g^{-1}).[43] The improvement of C_s is attributed to the following aspects: (1) the direct growth of Co_3O_4 onto the interconnected Ag ligaments ensures direct conductive contact, which facilitates electron transfer. (2) The porous nanostructure throughout the whole sheet provides a very high specific surface area. (3) The continuous open porosity ensures electrolyte access to all pores.

Fig. 6d shows Nyquist plots of the PSTS/Co_3O_4 electrodes with different Co_3O_4 loadings of 1.4, 2.9, 3.8 and 6.6 mg/cm^2. A plot consists of a semicircle at high frequency region and a straight line at low frequency region. The semicircle in the high frequency region corresponds to Faradic charge-transfer resistance (R_{ct}) that is related to the electroactive surface area of the electrode. The bulk resistance (R_b) is due to the combination of ionic and electronic resistances, intrinsic resistance of the active Co_3O_4 electrode and diffusive as well as contact resistance at the Co_3O_4 electrode/current collector interface. Through fit analysis of Nyquist plots, R_{ct} values are 0.40, 0.56, 1.01, and 1.12 Ω for the composite electrodes with 1.4, 2.9, 3.8 and 6.6 mg/cm^2 Co_3O_4, respectively. From the points intersecting with the real axis in the range of high frequency, the related R_b values are 0.33, 0.45, 0.80 and 0.89 Ω. Both R_{ct} and R_b increase with the loading of Co_3O_4, and the increase are especially large after the optimum, which supports that (1) the lack of electric contact between outlayer active materials with PSTS results in an obvious increase in resistance when the concentration is higher than 8 mM, which is consistent with SEM results. A sudden increase of the R_{ct} leads to (2) decrease electrolyte access and (3) decrease overall access to pores.

The CD curves of the optimal PSTS/Co_3O_4 composite measured at different current densities (Fig. S4) are nearly symmetric, demonstrating excellent electrochemical reversibility (Coulombic efficiency). Fig. 7a shows the corresponding C_s values at different current densities. Specific capacitances are 1276, 1139, 1013 and 986 F g^{-1} at 1.0, 2.0, 5.0, and 10 A g^{-1}, respectively. At a high current density of 10 A g^{-1}, the composite still has 986 F g^{-1} (77% of the capacitance at 1.0 A g^{-1}), in particular, there is only a small capacitance decrease when the current density creases from 5 to 10 A g^{-1} (almost parallel to the x-axis), making it very promising for rapid charge-discharge applications. Galvanostatic cycling is used to investigate the cycling stability. Fig. 7b shows 2000 charge-discharge cycles of the optimal electrode at a current density of 2 A g^{-1}. The electrode exhibits an excellent reversibility and cycling stability, retaining still 92% of the initial capacitance after 2000 cycles.

The high capacitances and charge/discharge rates offered by such hybrid structures make them promising candidates as electrodes in supercapacitors combining high-energy storage densities with high levels of power delivery. One should note that the porosity and Co_3O_4 content were not yet both optimized together. Since the optimum Co_3O_4 content was explained by ligament surface area coverage as well as that any addition of Co_3O_4 decreases the pore diameters, one must expect that different choices of the etching parameters and subsequent re-optimization of the Co_3O_4 content will result in even better performing electrodes.

4. Conclusions

We demonstrate a novel method for large-scale fabrication of PSTS. The porosity distributes throughout the whole volume, and the size of the pores decreases toward the inside. The porosity can be tailored by the acid concentration and etching time. The PSTS were used as highly conductive substrates for growth of Co_3O_4 capacitive material. The PSTS/Co_3O_4 electrode with optimized Co_3O_4 covering of the Ag network ligaments exhibits high specific capacitance of 1276 F g^{-1} at 1 A g^{-1}, which is much higher than previously reported values for pure Co_3O_4 nanostructures with different shapes, and even higher than those for Ag-Co_3O_4 composite nanowire array electrodes. Also, the electrode has a superior rate capability. As discussed, further research into optimal etching parameters and re-optimization of the Co_3O_4 content is bound to further improve the performance of the electrodes. Our new method of obtaining porous thin sheets can be extended to all materials that can be synthesized into sponges including many metals and even alloys.[44]

Supporting information

† Electronic supplementary information (ESI) available: SEM images (Fig. S1) showing surface morphology of a pressed silver thin sheet before etching, SEM images of the products after 5 min chemical etching of a silver sheet obtained by pressing silver NPs, and a commercial silver sheet (Fig. S2), and XRD pattern of the PSTS/Co_3O_4 composite (Fig. S3). CD curves at different current densities of the optimal PSTS/Co_3O_4 composite electrode (Fig. S4).

Author information

Corresponding authors

* Correspondence and requests for materials should be addressed to S.C. Tang (tangsc@nju.edu.cn) or X.K. Meng (mengxk@nju.edu.cn).

Conflict of interest

The authors declare no competing financial interest.

Acknowledgements

The authors kindly acknowledge the joint support by the PAPD (No. 50831004), the Fundamental Research Funds for the Central Universities, the Innovation Fund of Jiangsu Province (No. BY2013072-06), the Natural Science Foundation of Jiangsu Province (No. 2012729), the National Natural Science Foundation of China (No. 11374136), and the State Key Program for Basic Research of China (No. 2010CB631004).

References

1 B. C. Tappan, S. A. Steiner and E. P. Luther, *Angew. Chem. Int. Ed.*, 2010, **49**, 4544-4565.

2 J. Zhang and C. M. Li, *Chem. Soc. Rev.*, 2012, **41**, 7016-7031.

3 C. Z. Zhu, S. J. Guo and S. J. Dong, *Chem. Eur. J.*, 2013, **19**, 1104-1111.

4 S. Cherevko, N. Kulyk and C. H. Chung, *Nanoscale*, 2012, **4**, 103-105.

5 L. Y. Chen, J. S. Yu, T. Fujita and M. W. Chen, *Adv. Funct. Mater.*, 2009, **19**, 1221-1226.

6 H. J. Qiu, J. L. Kang, P. Liu, A. Hirata, T. Fujita and M. W. Chen, *J Power Sources*, 2014, **247**, 896-905.

7 X. Y. Lang, H. Y. Fu, C. Hou, G. F. Han, P. Yang, Y. B. Liu and Q. Jiang, *Nat. Commun.*, 2013, **4**, 2169-2173.

8 X. Chen, K. Sun, E. S. Zhang and N. Q. Zhang, *RSC Adv.*, 2013, **3**, 432-437.

9 H. J. Qiu, Y. Ito and M. W. Chen, *Scripta Mater.*, 2014, **89**, 69-72.

10 P. K. Matthew, W. J. Benjamin, D. O. Markus, J. F. Stephen, B. R. David, S. Vitalie, J. W. Gregory and A. Ilke, *J. Am. Chem. Soc.*, 2011, **133**, 9144-9147.

11 Y. G. Zhou, S. Yang, Q. Y. Qian and X. H. Xia, *Electrochem. Commun.*, 2009, **11**, 216-219.

12 C. Xu, Y. Liu, J. Wang, H. Geng and H. Qiu, *J. Power Sources,* 2012, **199**, 124-131.

13 N. Leventis, N. Chandrasekaran, A. Sadekar, G. S. Mulik and C. Sotiriou-Leventis, *J. Mater. Chem.*, 2010, **20,** 7456-7471.

14 N. C. Bigall, A. K. Herrmann, M. Vogel, M. Rose, P. Simon, W. Carrillo-Cabrera, D. Dorfs, S. Kaskel, N. Gaponik and A. Eychmller, *Angew. Chem. Int. Ed.*, 2009, **48**, 9731-9734.

15 C. Fang, A. V. Ellis and N. H. Voelcker, *J. Electroanal. Chem.*, 2011, **659**, 151-160.

16 P. G. Kuzmina, G. A. Shafeeva, G. Viaub, B. Warot-Fonrosec, M. Barberogloud, E. Stratakisd and C. Fotakis, *Appl. Surf. Sci.*, 2012, **258**, 9283-9287.

17 Y. Li, W. Z. Jia, Y. Y. Song and X. H. Xia, *Chem. Mater.*, 2007, **19**, 5758-5764.

18 P. N. Bartlett, J. J. Baumberg, P. R. Birkin, M. A. Ghanem and M. C. Netti, *Chem. Mater.*, 2002, **14**, 2199-2208.

19 P. Giorgio, M. Michele and D. Francesco, *Scripta Mater.*, 2014, **76**, 57-60.

20 T. T. Song, Y. L. Gao, Z. H. Zhang and Q. J. Zhai, *Corros. Sci.*, 2013, **68**, 256-262.

21 J. F. Huang and I. W. Sun, *Adv. Funct. Mater.*, 2005, **15**, 989-994.

22 S. Cherevko, X. Xing and C. H. Chung, *Electrochem. Commun.*, 2010, **12**, 467-470.

23 K. Y. Niu, S. A. Kulinich, J. Yang, A. L. Zhu and X. W. Du, *Chem. Eur. J.*, 2012, **18**, 4234-4241.

24 A. Gutes, C. Carraro and R. Maboudian, *J. Am. Chem. Soc.*, 2010, **132**, 1476-1477.

25 H. Won, N. Hayk, W. C. Whan, J. M. Lee and J. S. Hwang, *Chem. Eng. J.*, 2010*,* **156**, 459-464.

26 Z. Q. Li, B. Q. Li, Z. X. Qin and X. Lu, *J. Mater. Sci.*, 2010, **45**, 6494-6497.

27 H. Z. Lu, *Powder Technol.*, 2012, **203**, 176-179.

28 X. J. Li, H. Liu, Y. Wang, X. M. Wu, Z. P. Chu and R. Lu, *Corros. Sci.*, 2014, **84**, 159-164.

29 S. P. Zhu, S. C. Tang and X. K. Meng, *Chin. Phys. Lett.*, 2009, **26**, 078101.

30 X. C. Dong, *ACS Nano*, 2012, **6**, 3206-3213.

31 X. Y. Lang, A. Hirata, T. Fujita and M. W. Chen, *Nat. Nanotech.*, 2011, **6**, 232-236.

32 J. L. Liu, L. L. Zhang, H. B. Wu, J. Y. Lin, Z. X. Shen and X. W. Lou, *Energy Environ. Sci.*, 2014, **7**, 3709-3719.

33 J. L. Liu, J. Sun and L. Gao, *J. Phys. Chem. C*, 2010, **114**, 19614-19620.

34 S. Vijayakumar, A. Kiruthika, Ponnalagi S. Nagamuthu and G. Muralidharan, *Electrochim. Acta,* 2013, **106**, 500-505.

35 S. Xiong, C. Yuan, X. Zhang, B. Xi and Y. Qian, *Chem. Eur. J.*, 2009, **15**, 5320-5326.

36 X. H. Xia, J. P. Tu, X. L. Wang, C. D. Gu and X. B. Zhao, *Chem. Commun.*, 2011, **47,** 5786-5788.

37 J. Xu, L. Gao, J. Cao, W. Wang and Z. Chen, *Electrochim. Acta*, 2013, **56**, 732-736.

38 M. Sun, S. Vongehr, S. C. Tang, L. Chen, Y. G. Wang and X. K. Meng, *Mater. Lett.*, 2015, **141**, 165-167.

39 Y. H. Xiao, S. J. Liu, F. Li, J. H. Zhao, S. M. Fang and D. Z. Jia, *Adv. Funct. Mater.*, 2012, **22**, 4052-4059.

40 G. X. Wang, X. P. Shen and J. Horvat, *J. Phys. Chem. C*, 2009, **11**, 4357-4361.

41 F. Y. Ning, M. F. Shao and C. L. Zhang, *Nano Energy*, 2014, **7**, 134-142.

42 Y. Xu, J. C. Huang and L. Cheng, *Appl. Mech. Mater.*, 2013, **268-270**, 157-63.

43 H. Cheng, G. L. Zhou, Q. D. Jian, C. Y. Chung, K. Zhang and Y. Y. Li, *Nano Res.*, 2010, **3**, 895-901.

44 S. C. Tang, S. Vongehr, Y. G. Wang and X. K. Meng, *J. Mater. Chem. A*, 2014, **2**, 3648-3660.

Figures and figure captions

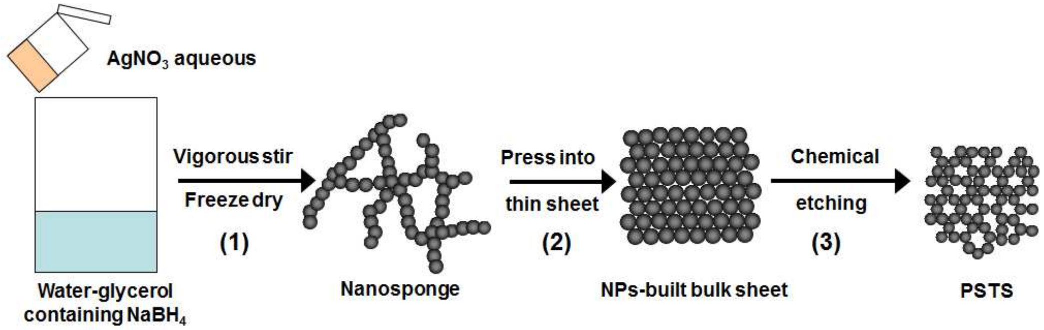

Scheme 1 The preparation of PSTS includes three main steps: (1) synthesis of silver nanosponges with 3D network-like nanostructure in ethanol-glycerol mixed solution, (2) pressing the sponges into thin sheets, and (3) chemical etching.

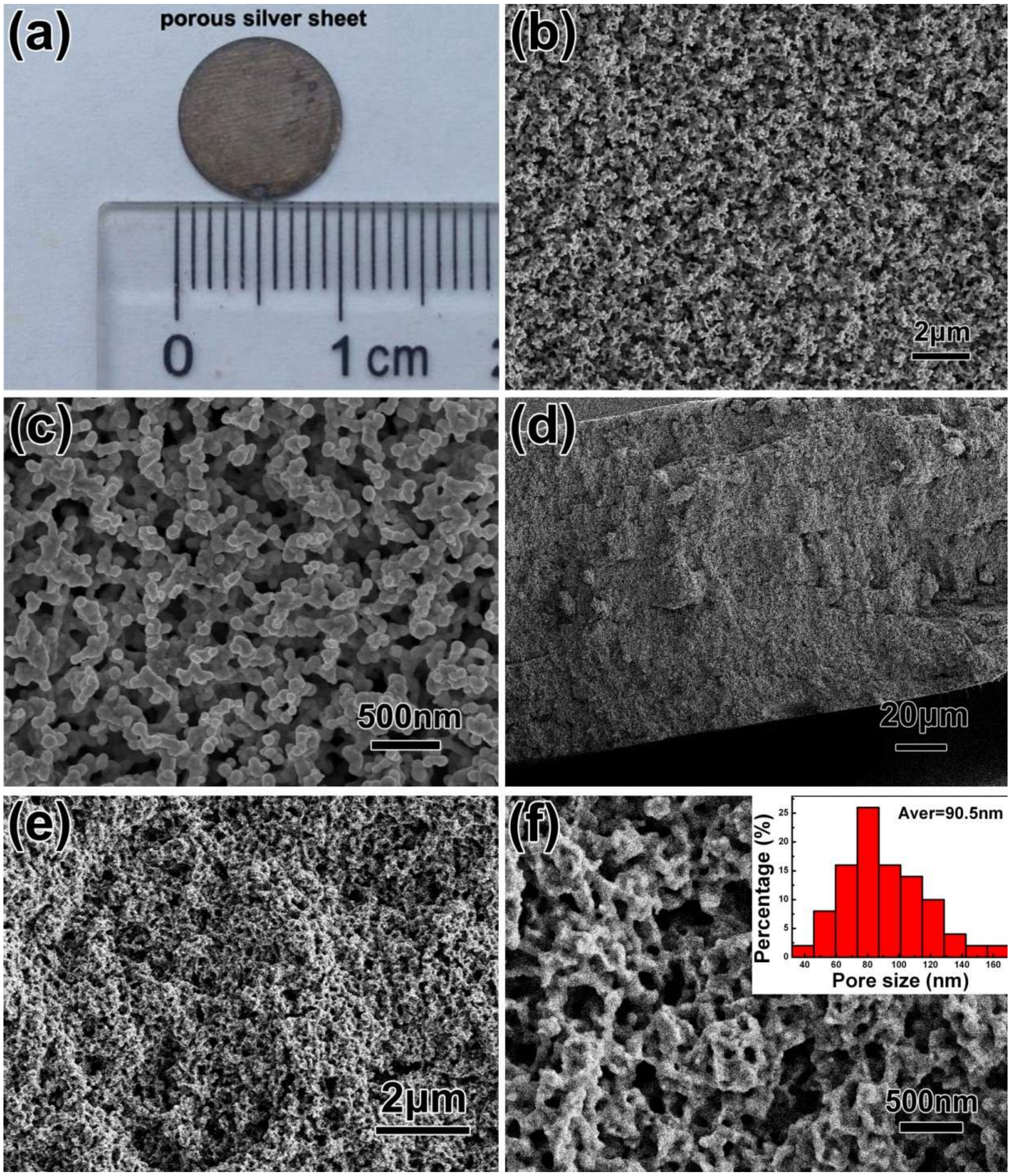

Fig. 1 (a) A photograph of a porous silver sheet obtained from 5 min etching in 16% HNO_3, (b-c) SEM images of the top surface, and (d-f) views of the cross-section of the broken sheet. The inset of 1f is a histogram of diameters for 50 pores in the cross-section.

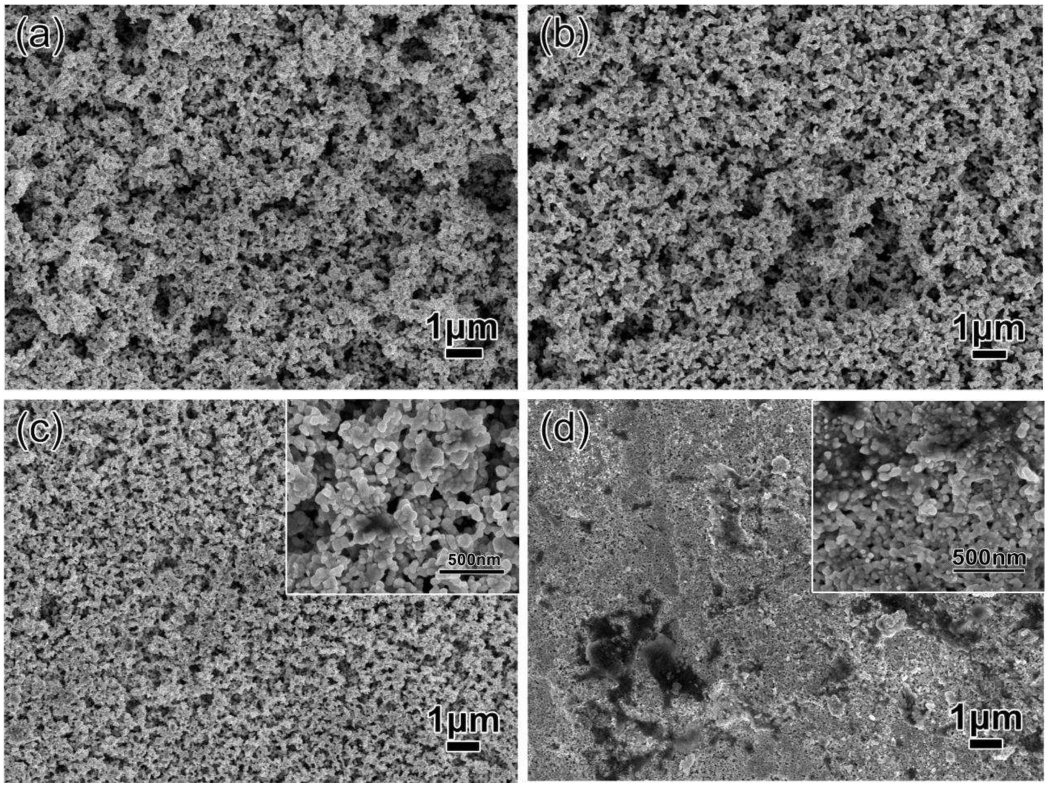

Fig. 2 SEM images showing surface morphologies of PSTS obtained using HNO_3 concentrations of (a) 32%, (b) 20%, (c) 10%, and (d) 5% after 4 min etching. The insets in 2c-d are magnified SEM images; the one in 2d is however taken after one more hour inside the etching solution.

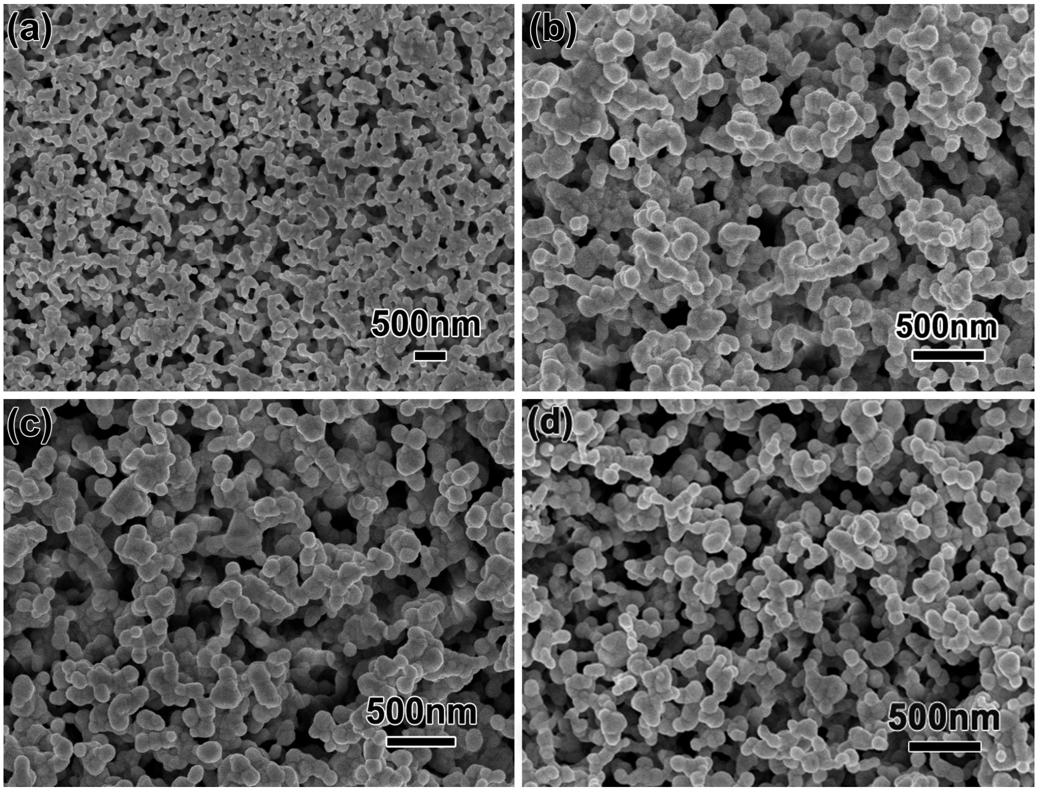

Fig. 3 SEM images showing the surfaces of pressed silver sheets after etching in 16% HNO_3 for (a) 1, (b) 2, (c) 3, and (d) 4 min.

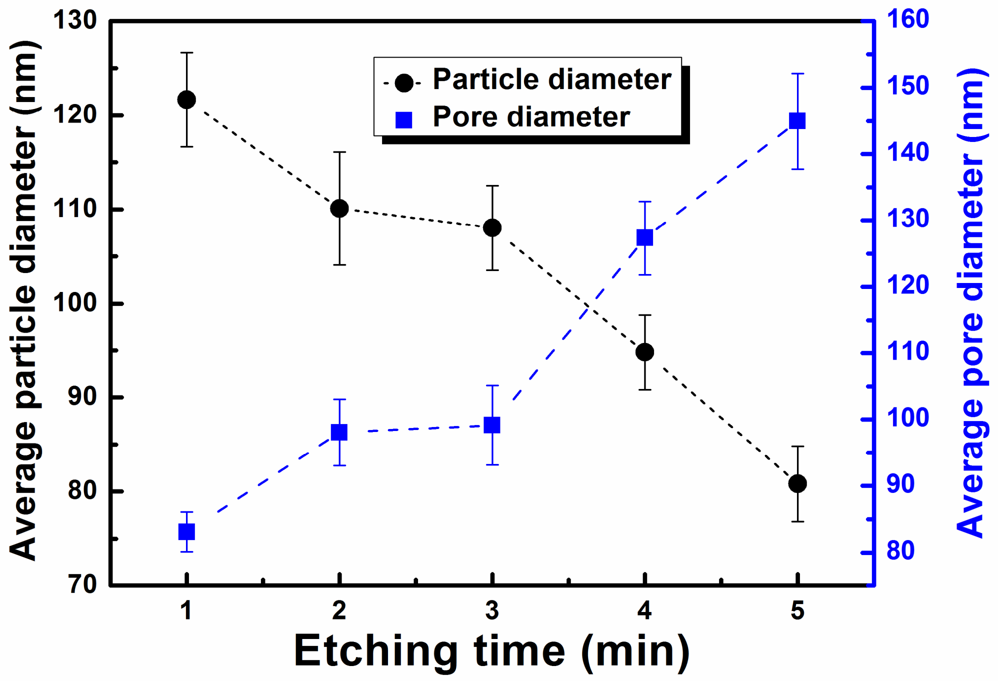

Fig. 4 Average diameter of ligament NPs and pore diameters (all measured at the surface of the PSTS) versus etching time in 16% HNO_3.

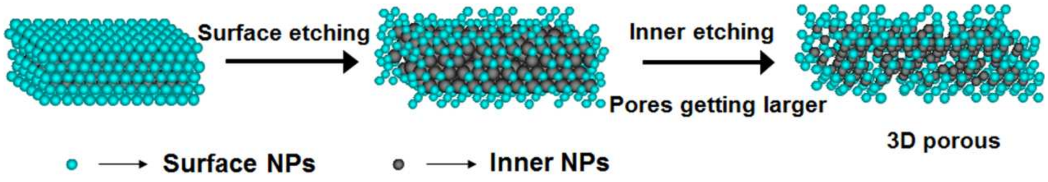

Scheme 2 Formation of PSTS with their porous nanostructure during chemical etching from a pressed silver sheet.

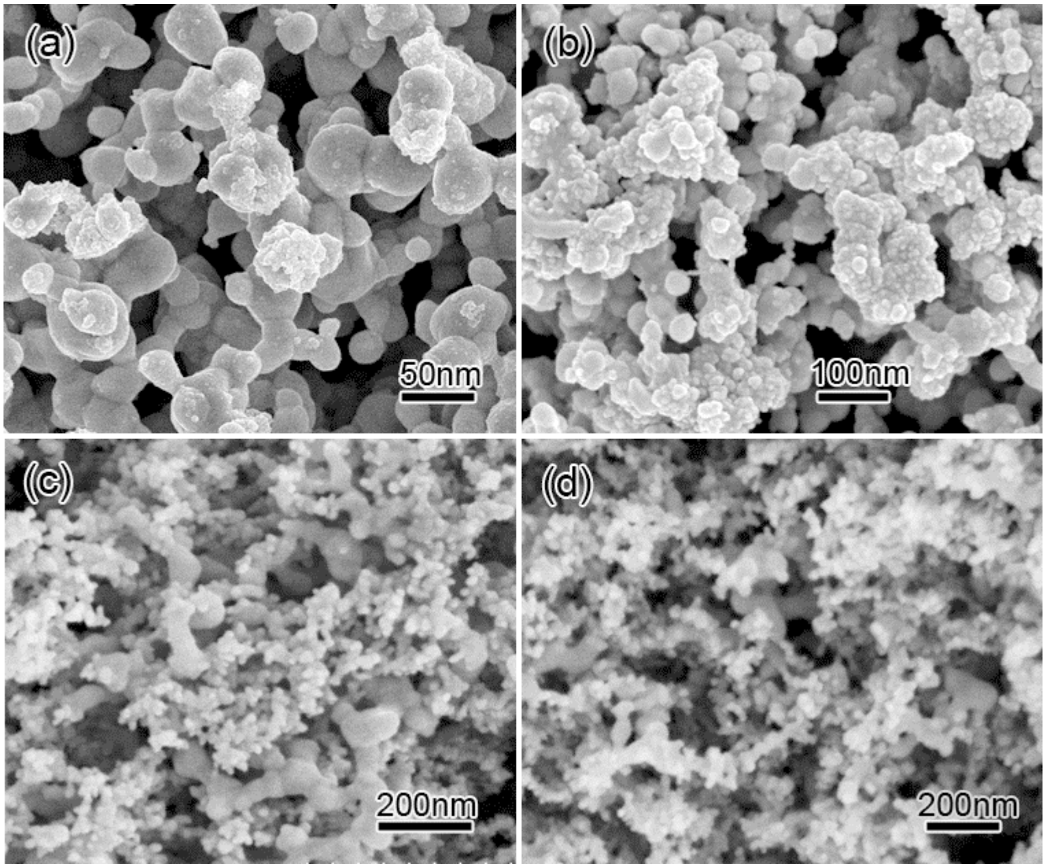

Fig. 5 SEM images of PSTS/Co_3O_4 composites obtained with Co^{2+} concentrations of (a) 1 mM, (2) 8 mM, (c) 16 mM, and (d) 20 mM.

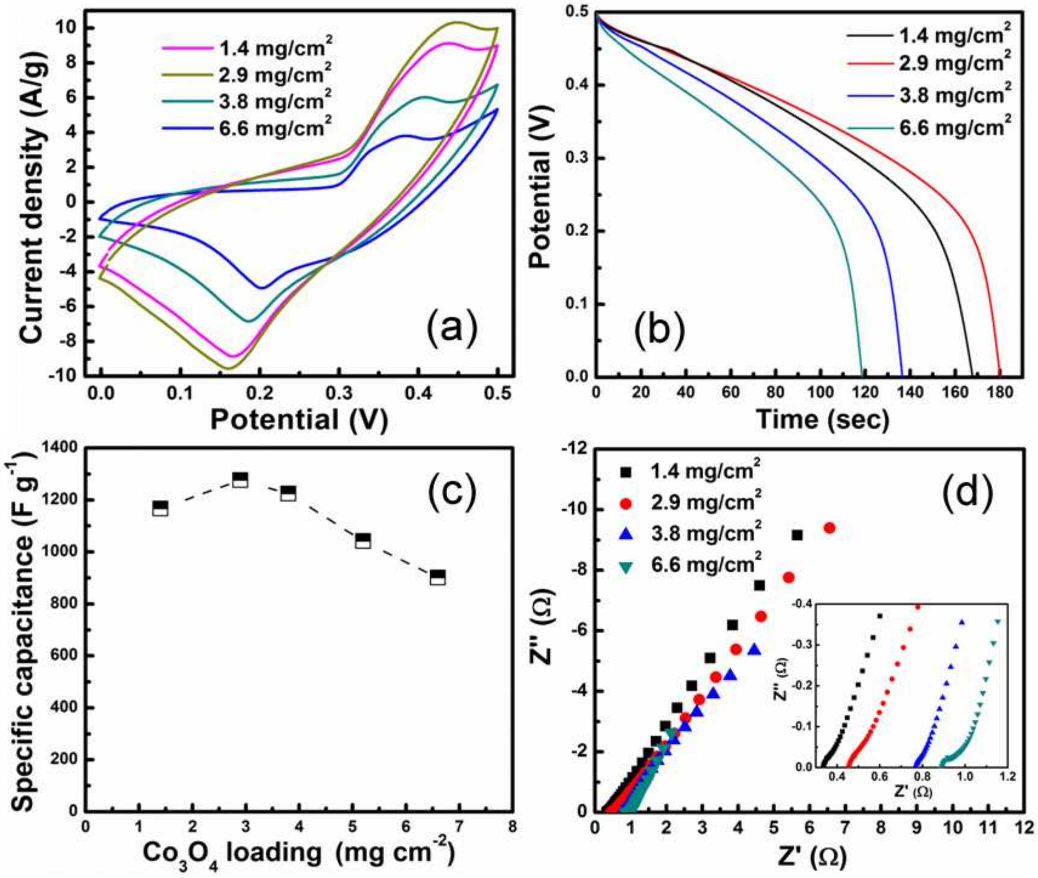

Fig. 6 (a) CV curves measured at a scan rate of 5 mV/s, and (b) Discharge curves at a current density of 1.0 A/g, (c) corresponding specific capacitances, and (d) EIS curves of the PSTS/Co_3O_4 composites obtained at Co^{2+} concentrations of 5, 8, 10, and 20 mM, resulting in Co_3O_4 loadings of 1.4, 2.9, 3.8, and 6.6 mg/cm^2, respectively.

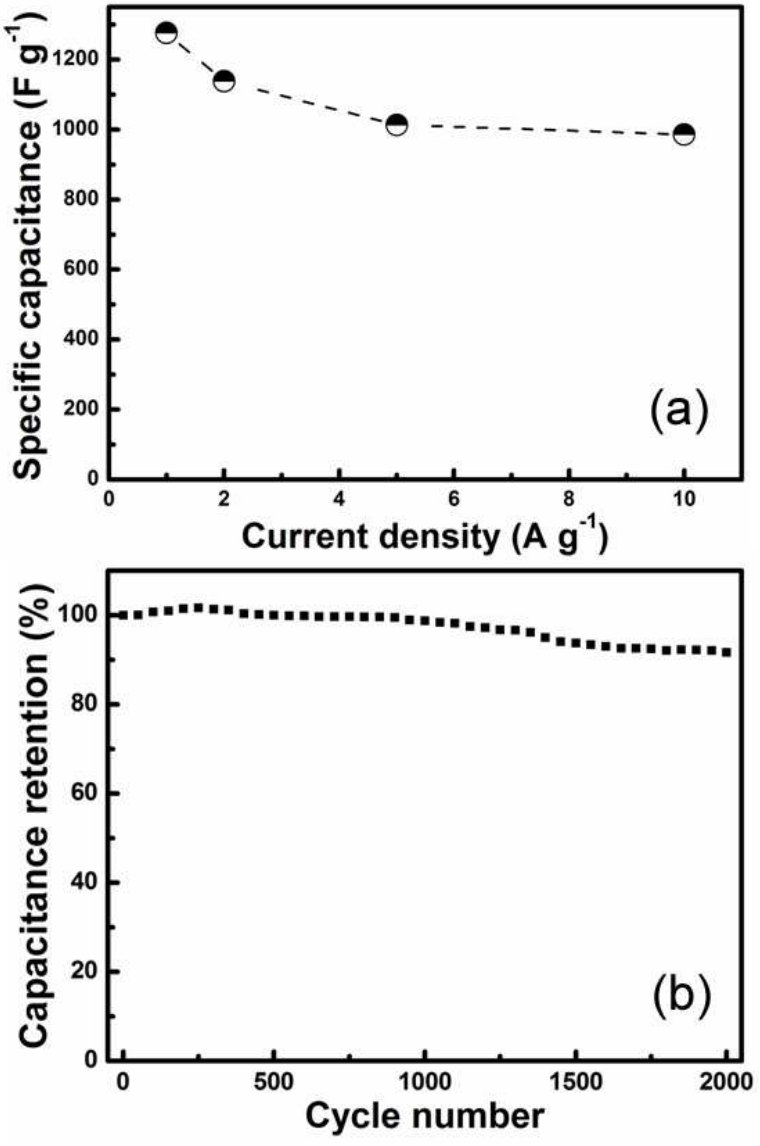

Fig. 7 (a) specific capacitances obtained at different current densities, and (b) cycling stability test over 2,000 cycles of the optimal PSTS/Co_3O_4 composite electrode with the Co_3O_4 loading of 2.9 mg/cm^2.